Faraday Discussions

Cite this: DOI: 10.1039/d5fd00129c

ROYAL SOCIETY OF CHEMISTRY

PAPER

View Article Online
View Journal

Surface orientation-dependent electro-oxidation of a polycrystalline gold electrode

Auden Ti, *[a] Hanna Sjö, *[a] Andrea Grespi, [a] Estephania Lira, [a] Alfred Larsson, [b] Ulrike Küst, [a] Claire Berschauer, [ac] Johan Gustafson, [a] Lindsay R. Merte, [d] Jan Knudsen [a] and Edvin Lundgren *[a]

Received 28th November 2025, Accepted 2nd January 2026

DOI: 10.1039/d5fd00129c

The activity and stability of an electrocatalyst is governed by the structural and chemical changes occurring at the solid–liquid interface. While single crystal electrodes have often served as model systems to elucidate structure–function relationships, extending these insights to more realistic polycrystalline electrodes requires experimental techniques with spatial resolution that can operate under electrochemical conditions. Herein, the electro-oxidation of a polycrystalline gold electrode is investigated *in situ* using two-dimensional surface optical reflectance, electrochemical near ambient pressure X-ray photoelectron spectroscopy, and tomographic surface X-ray diffraction. This combination of techniques provides surface-sensitive chemical and structural information. In the case of the polycrystalline gold, a surface orientation-dependent oxidation behaviour is found where both the onset and growth of oxides/hydroxides are affected. Our approach provides an enhanced understanding of the dynamic behaviour of complex electrodes under harsh environments, enabling grain-resolved insight into electrochemical processes.

Introduction

Understanding the electrochemical (EC) behaviour of noble metals under oxidising conditions is essential for a rational design of better electrocatalysts for applications such as proton exchange membrane electrolysers and fuel cells.[1,2] The surfaces of these catalytic materials undergo dynamic structural and compositional changes under reaction conditions, including oxidation,

---

[a] *Division of Synchrotron Radiation Research, Lund University, Lund, Sweden. E-mail: auden.ti_yun@fysik.lu.se; hanna.sjo@fysik.lu.se; edvin.lundgren@fysik.lu.se*

[b] *Leiden Institute of Chemistry, Leiden University, Leiden, Netherlands*

[c] *Wallenberg Material Science Initiative for Sustainability, Division of Synchrotron Radiation Research, Lund University, Lund, Sweden*

[d] *Department of Materials Science and Applied Mathematics, Malmö University, Malmö, Sweden*

dissolution, and restructuring of active sites.[3,4] Hence, *in situ* and *operando* characterisations of electrode surfaces under realistic EC conditions are crucial to establish structure–function relationships.[2] Au electrodes are often used as model systems in this context due to their well understood EC features, allowing for association between EC behaviour and observed surface structural and compositional changes. Many EC processes, such as water splitting and the oxidation of CO or other chemicals, are closely related to the oxidation of the electrocatalyst, and Au electrodes have been used for fundamental studies and experimental benchmarking.[5–7] It has in previous studies been argued that the oxidation of the electrocatalyst is linked to dissolution and instabilities,[8] even for corrosion resistant alloys[9] and noble metals.[10,11]

In this context, low-index single crystals have frequently been used as model electrodes,[12–16] while industrial materials are in general polycrystalline. To mimic such materials, high-index surfaces with a more complex surface structure can be used,[17–19] and facile oxidation at steps,[19] for example, have been reported. An alternative is to directly study polycrystalline samples, in which the model electrode consists of grains with various crystalline orientations. Such an electrode would enable a direct comparison of different surface orientations between grains under the same EC conditions. A polycrystalline surface, however, introduces the additional requirement of spatial resolution on the applied experimental techniques.

Surface reconstructions have often been studied with excellent spatial resolution using traditional electron-based methods, which, due to the short mean free path of electrons, are in most cases limited to low pressure environments. Traditional EC methods, such as cyclic voltammetry (CV) only provide indirect information about changes in the surface structure and lack spatial resolution, with some exceptions.[5] Scanning probe microscopy (SPM) may also be used in liquids,[5] but can suffer from instabilities under oxidation conditions, primarily due to bubble formation, surface wettability, electrolyte evaporation and tip degradation.[20] Photoemission electron microscopy (PEEM) provides chemical information of the surface with spatial resolution, but is limited to pressures of 10^{-5} mbar,[21] though higher pressures have been reached.[22] Surface X-ray diffraction (SXRD) has been used to study reactions at electrode surfaces,[12] provides sufficient surface sensitivity and, as a photon-in, photon-out method, has no issues with penetration of the electrolyte, but has no spatial resolution. Electrochemical near ambient pressure X-ray photoelectron spectroscopy (EC-NAPXPS) may also be applied to EC systems through the so-called dip-and-pull method but is typically limited in spatial resolution.[23]

In this contribution, we characterise the surface orientation-dependent oxidation of a polycrystalline Au surface with three different surface sensitive *in situ* techniques, with spatial resolution. The first technique, two-dimensional surface optical reflectance (2D-SOR), provides a direct image of the surface with a lateral resolution around 5 μm and high temporal resolution, which allows us to follow changes in the reflectance that can be related to surface oxidation. The small X-ray beam at the HIPPIE beamline at MAX IV (50 μm) and precise sample manipulation enables spatially resolved EC-NAPXPS which provides grain specific spectroscopic data, revealing the presence or absence of oxides/hydroxides† on

---

† Oxide/hydroxide will be used throughout the contribution due to the uncertain nature of the specific oxidised Au species formed.

the surface. Finally, with tomographic SXRD (TSXRD), we follow the roughening of individual grains during oxidation. Either potential step experiments or CV were performed in parallel with all three methods. Although the CV measurements lack spatial resolution, they are used as electrochemical reference points to link the different surface sensitive experiments together.

We show with EC-NAPXPS that differences in the 2D-SOR reflectance observed for the different grains during electro-oxidation correspond to surface oxidation at different potentials for each grain. Thus, the change in the 2D-SOR reflectance can be explained by the difference in refractive indices for metallic and oxidised Au. The thicknesses of the oxides/hydroxides formed on each grain can be calculated using the refractive indices of bulk Au and Au_2O_3, the change in reflectance, and Fresnel's equations. These calculations can then be compared to the corresponding thickness values obtained by EC-NAPXPS. The intensity variations in the TSXRD have a similar behaviour to the 2D-SOR but exhibit differences that reflect the distinct sensitivities of the techniques.

Methods

Sample

The polycrystalline Au sample (Surface Preparation Laboratory) has a surface diameter of 7.5 mm. It has a hat-shape with 4 mm height and 14 mm base diameter. The sample was initially mirror polished. For the 2D-SOR experiments, the sample was cleaned in nitric acid, rinsed in ultrapure water (mQ, 18.2 MΩ), and finally flame annealed and cooled in air.[24] For the EC-NAPXPS and TSXRD experiments, the sample was flame annealed and subsequently cooled in air.

EBSD

The electron backscatter diffraction[25] (EBSD) measurements were performed at the Department of Geology at Lund University using an Oxford Instruments Symmetry S2 detector connected to a high-resolution field emission scanning electron microscope (FE-SEM; Tescan Mira3) and Oxford Instruments AZtec software for data collection. The scan was performed with a 30 μm step size, 20 kV accelerating voltage, and a 70° stage tilt.

2D-SOR

2D-SOR is a method for studying changes at a surface.[26–28] By measuring the reflected light from a light-emitting diode (LED) incoming at normal incidence, oxide thicknesses down to 2–3 Å can be detected.[29] 2D-SOR can be used to study samples in high-pressure environments or liquids, if there is optical access to the sample, and can be used for *operando* studies of polycrystalline surfaces[30–32] with a lateral resolution of approximately 5 μm. More details of the method can be found in ref. 28.

The 2D-SOR setup, illustrated in Fig. 1, consists of a 660 nm red LED (Thorlabs M660L4), and the reflected light was measured using a 1936 × 1216 pixel, 12-bit monochrome complementary metal oxide semiconductor (CMOS) camera (uEye UI-3260CP). The EC measurements were performed using the polyether-ether-ketone (PEEK) EC flow cell described in ref. 32. The cell is a three-electrode system, with the polycrystalline Au sample as the working electrode, a Au rod

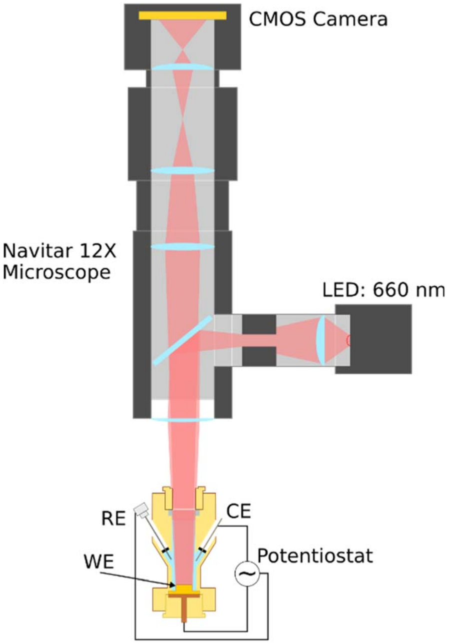

Fig. 1 Drawing of the 2D-SOR setup for EC measurements. Red (λ: 660 nm) LED light is shone on the polycrystalline Au sample (WE), and the reflected light from the sample is measured using a CMOS camera. The microscope system allows for the CMOS camera to be focused on the sample surface. Figure adapted from ref. 32, under CC-BY 4.0 license.

as the counter electrode, and leakless miniature saturated Ag/AgCl (eDAQ, ET072) as the reference electrode. The CV was performed in 0.1 M H_2SO_4 with a potential range of -0.1 to 2.0 V_{RHE}, at scan rate of 20 mV s^{-1}.

EC-NAPXPS

The EC-NAPXPS measurements were performed at the HIPPIE beamline at MAX IV in Lund, Sweden[33] using the dip-and-pull method.[23] HIPPIE is a soft X-ray beamline that offers a dedicated solid–liquid endstation for EC dip-and-pull experiments in a vacuum chamber with a controlled gaseous environment of 5×10^{-6} mbar up to 30 mbar. The chamber consists of a top manipulator where the EC sample holder can be mounted and a bottom manipulator that holds a beaker filled with electrolyte cooled to 10 °C using a water-cooled copper plate.

The PEEK EC sample holder functions as part of a 3-electrode setup shown in Fig. 2, where the working electrode (the polycrystalline Au sample) is secured to the sample holder. The sample was, together with the counter (Pt foil) and reference (leakless miniature Ag/AgCl, eDAQ ET072-1) electrodes, dipped into the electrolyte beaker filled with degassed 0.05 M H_2SO_4 for EC measurements using a Bio-Logic SP200 potentiostat. A controlled background pressure of approximately 14 mbar of water vapour was applied during the measurements. The electrodes were dipped into the electrolyte (Fig. 2a) and held at a potential before subsequently being pulled out of the electrolyte and brought near the photoelectron analyser (Fig. 2b).[23,34] A coordinate system (Fig. 2c) for the incident

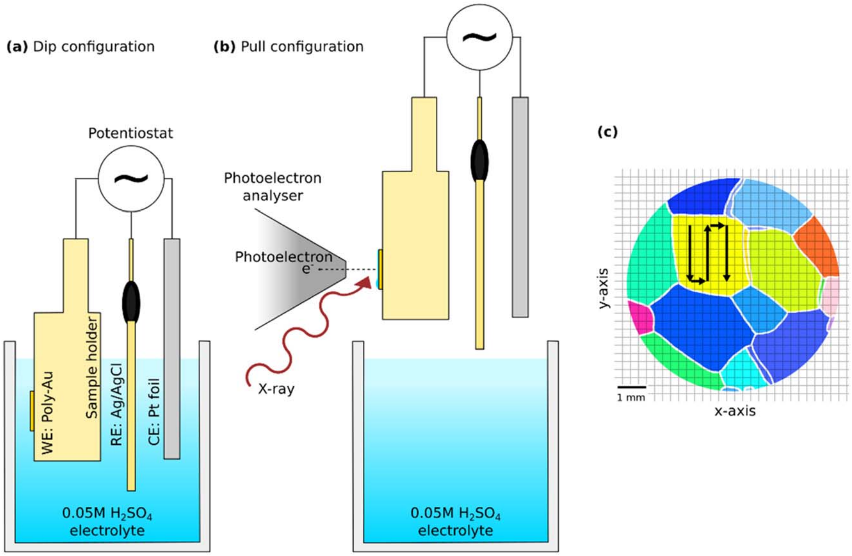

Fig. 2 The experimental procedure in ambient pressure environment. (a) The electrodes are dipped, and EC measurements are performed. (b) The electrodes are pulled out of the electrolyte for XPS measurements. (c) The movement of the sample (working electrode) while probing with XPS (black arrows indicate the probing path). A coordinate system was established from the identified grains from EBSD.

photon beam was created. During XPS measurements, the sample was moved continuously to minimise beam-induced effects.

The XPS spectra were measured in normal emission using an incident photon energy of 1200 eV, with a beamline slit size of 1 μm, and pass energy of 100 eV for the Au 4f core level. The incident photon beam size of 50 μm was small enough to resolve individual grains of our polycrystalline Au surface. Peak fitting of the XPS spectra was performed using Python and the LMFIT package.[35] More details are available in supplementary information (SI) Section 6.

Initially, each grain was probed with XPS at open circuit potential (OCP) conditions, where the electrodes were dipped and pulled without any applied potential. For applied potential measurements, a CV was first performed with a potential range of 0.25–1.85 V_{RHE} at 50 mV s^{-1} and subsequently polarised until a steady-state current was reached before pulling the electrodes out for XPS measurements of each grain. The applied potentials were 1.4 V_{RHE}, 1.5 V_{RHE}, 1.6 V_{RHE}, and 1.7 V_{RHE}. An example of a full EC measurement procedure for a grain is shown in SI Section 5.

TSXRD

TSXRD is an extension of SXRD[36,37] where diffraction signals from the polycrystalline surface are assigned to the grains of the surface to circumvent the lack of spatial resolution of SXRD. The assigned crystal truncation rods (CTRs) or super lattice rods (SLRs) can then be studied as in conventional SXRD studies. The diffraction measurements were performed at the Swedish Materials Science Beamline (P21.2) at PETRA III at DESY in Hamburg.[38] The X-ray photon energy was 38 keV and the spot size was 100 × 20 μm (horizontal × vertical). An angle of incidence of 0.11° was used, which is just below the critical angle for total reflection for Au at this X-ray energy. This angle resulted in a beam footprint covering the length of the sample. When measuring CTRs, a Pb mask was placed over the detector with rings covering all Bragg spots for the first four Debye–Scherrer rings of Au at this beam energy and sample–detector distance (Fig. 3b).

The same PEEK EC flow cell as described for the 2D-SOR experiment was used (Fig. 3a), which has been described in previous studies.[39,40] The three-electrode setup consisted of the polycrystalline Au sample as the working electrode, a Pt rod as the counter electrode, and a mini hydrogen reference electrode (Mini-HydroFlex, Gaskatel). The CV was performed in 0.05 M H_2SO_4 with a potential range of 0.2–1.75 V_{RHE}, at a scan rate of 10 mV s^{-1}. During the TSXRD measurements, fresh electrolyte was constantly flowed through the cell using inflow and outflow peristaltic pumps (Masterflex L/S Easy-Load II).

The sample surface was mapped at OCP with tomographic grazing incidence X-ray diffraction (TGIXRD) as described in ref. 41. For this, a repetitive rotational measurement was performed, measuring the Bragg reflections. The repetitive measurement procedure consists of a series of single rotational measurements with the beam at different offsets from the rotational axis (Fig. 3c and d), resulting in a measurement pattern where the whole sample is measured at a large angular range. Here, 77 rotational scans were performed between horizontal steps of 100 μm. Each rotational measurement was a 200° rotation during continuous measurements of 0.15 s exposures, corresponding to 0.5° per detector image. The resulting map provided coordinates for each grain during the subsequent

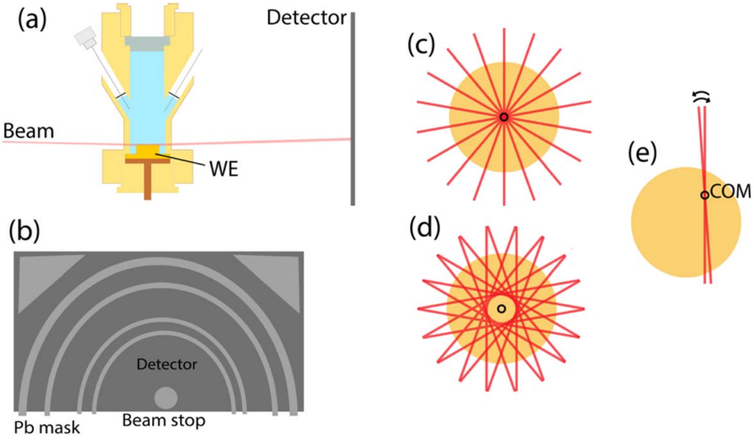

Fig. 3 Measurement procedure and setup for TSXRD. (a) A simplified drawing of the sample in the EC-cell. More details are shown in Fig. 1. (b) The detector masked with circular Pb mask to cover all Bragg spots. (c and d) The measurements procedure for the whole surface. While keeping the centre of rotation at the sample centre, the sample is moved such that the X-ray beam moves to different offsets from the sample centre as shown in d. The overlap of measurements with many of these offset rotations will provide a measurement of the whole surface at a large angular range. (e) The measurement procedure for the fast measurement. The centre of rotation is moved to the COM position of the grain of interest. The sample is then rotated back and forth for a small angular range covering a signal of interest.

measurements. The repetitive rotational measurement procedure was repeated with the Pb mask in place to measure the surface signals. The CTRs were assigned to grains by comparing their reciprocal positions to the Bragg reflections of the bulk structure and by studying their occurrence over the sample to the grain coordinates as further discussed in SI Section 1.

Diffraction was measured during separate runs of the CV for each grain of interest. In each run, a CV sweep was performed and a single CTR was measured during continuous azimuthal scans back and forth over a 4° range with the rotational axis at the centre of mass (COM) of the grain of interest (Fig. 3e). Each scan was measured with 8 exposures of 0.15 s during constant rotation, as above corresponding to 0.5° per image.

As a complement, a second experiment was performed, where the grains were measured in series using a scanning SXRD approach. Here, a CTR of each grain of interest was measured as above after each other. To keep the EC conditions more consistent between measurements, the scanning SXRD was measured while applying small polarisation steps of ∼5 minutes at potentials across the oxidation peaks (0.3–1.7 V_{RHE}), and then back to reducing potentials. These results are shown in Fig. S4.

Results

We have followed the electro-oxidation of a polycrystalline Au sample using 2D-SOR and TSXRD during CV, and EC-NAPXPS after applying constant polarisation. As a reference, Fig. 4a shows a map[42] of the surface with grain orientations characterised *ex situ* by EBSD. The study focuses on the three grains marked as 1–3. As shown by the stereographic triangle in Fig. 4a, the orientation of grain 1 is in between a (100) and a (110) orientation, corresponding to an open (210) surface orientation (Fig. 4b). Grain 2, which can be approximated as a (554) surface orientation, has larger (111) oriented terraces separated by (110) steps (Fig. 4c). Finally, grain 3 can be approximated as a (552) surface which has smaller (111) terraces and more prominent (110) steps, relative to grain 2 (Fig. 4d). Fig. 4e

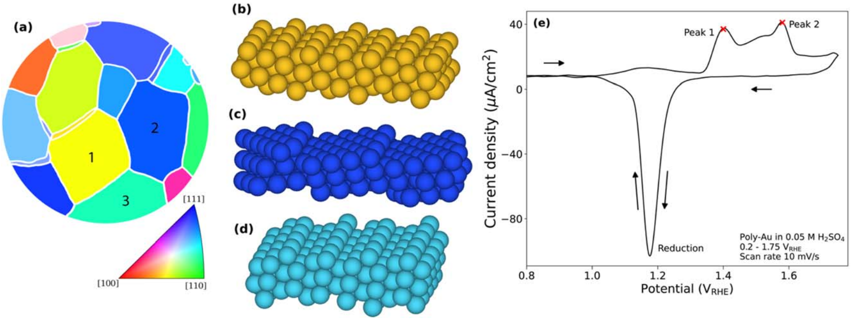

Fig. 4 (a) EBSD grain map of the polycrystalline Au sample with orientations defined in the triangle.[42] (b–d) Surface models of grains 1–3. (e) CV from the TSXRD experiment using the polycrystalline Au sample surface in 0.05 M H_2SO_4 with 10 mV s^{-1} scan rate. The red crosses mark the two main features within the oxidation peak. Arrows indicate the scan direction.

shows the CV of the polycrystalline Au sample, performed separately. As the measured current density includes contributions from all EC processes on all grains, we lack grain specific information. The main features of the CV are the broad positive feature between 1.3 and 1.6 V_{RHE} during increasing potential, indicating oxidation of the surface, and the sharper negative peak just below 1.2 V_{RHE} during decreasing potential, indicating reduction of the oxide/hydroxide. In addition, there is a weaker broad feature between 1 and 1.3 V_{RHE}, prior to the oxidation, which we relate to H_2O_2 oxidation[43] (SI Section 9). This reaction does not affect surface oxidation and will therefore not be discussed further here. The oxidation peak is broader than what is typically seen for single crystal gold electrodes.[44,45] Within this broad peak, two main peaks can be distinguished.

2D-SOR

To facilitate comparison between the different methods, we have chosen to present some published data[32] but have expanded the analysis to include the oxide thickness for the three grains of interests. Additionally, results from 10 grains can be found in SI Section 4. The 2D-SOR measurements are presented in Fig. 5. Note that Fig. 5a and b are adapted from ref. 32, but Fig. 5c is entirely new. In the representative 2D-SOR image in Fig. 5a, some of the grain boundaries are clearly visible and the three grains of interest are easily identified. Fig. 5b shows the normalised reflectance as a function of time, overlaid with the CV measured simultaneously. The normalised reflectance (R/R_0) is obtained by dividing the raw SOR reflectance (R) with the initial averaged SOR reflectance (R_0). From 30 s to 70 s, a slow linear decrease in reflectance is observed, which could be attributed to the charging/discharging of the electrochemical double-layer capacitance or

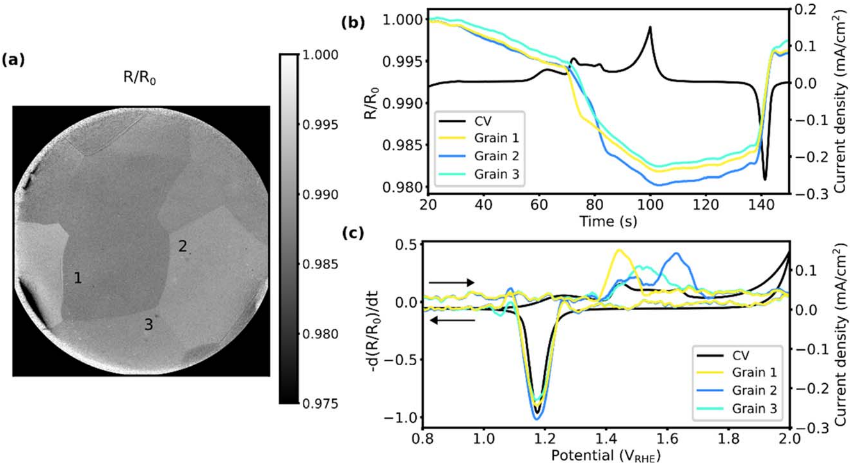

Fig. 5 2D-SOR of the three grains during CV. (a) A normalised 2D-SOR image of the surface at an applied potential of ~1.5 V_{RHE} with the grains marked, adapted from ref. 32, under CC-BY 4.0 license. (b) The normalised reflectance as a function of time for each grain, adapted from ref. 32, under CC-BY 4.0 license. (c) The negative time derivative of the normalised reflectance as a function of potential. The potential range of the CV was −0.1 to 2 V_{RHE} at 20 mV s^{-1} and performed in 0.1 M H_2SO_4. The arrows indicate scan direction.

adsorption/desorption of oxygenated species. When approaching the onset of the broad Au oxidation peak (70–85 s), a rapid drop in reflectance is observed for all grains, which returns close to the initial values after the onset of the reduction peak of the CV (~140 s). The decrease in reflectance observed for the grains suggests the formation of a surface Au oxide/hydroxide.

In Fig. 5c, the *y*-axis shows the negative time derivative of the normalised SOR reflectance, and the *x*-axis shows the CV potential. The derivative of the change in reflectivity reproduces the oxidation and reduction peaks in the CV (see Fig. S7a), suggesting a change in the refractive index of the surface upon oxidation and reduction. Furthermore, the potential for this change is different for each grain, which was also reported previously,[32] clearly showing that the surfaces respond differently to the EC conditions. The combined derivatives from the grains reproduce the CV nicely. In a simplified model, the measured current density from the CV is the sum of the current density of each grain. Furthermore, the current density of each grain is proportional to the oxide/hydroxide growth rate. Similarly, the change in normalised reflectance is proportional to the oxide thickness, and therefore its time derivative is proportional to the oxide/hydroxide growth rate. Note that an increase in the negative derivative of the reflectance represents a decrease in the reflectance.

The SOR signal can be used to estimate the oxide thickness using Fresnel's equations[28–30] (SI Section 3). The estimated oxide/hydroxide thicknesses of the three grains across the Au oxidation peak, assuming the growth of a homogeneous Au^{3+} oxide (Au_2O_3) film,[10] are presented in Fig. 6. Note that due to the lack of refractive index value in the literature for Au^{3+} oxyhydroxide ($HAuO_2$), the thickness is estimated using the refractive index of Au_2O_3. The initial oxidation step of grain 1 gives rise to an oxide thickness of ~2 Å and is followed by a steady increase to ~3.5 Å at the highest applied potential. Grain 2 exhibits a two-step increase in oxide thickness, first to ~1 Å, and next to ~3 Å, followed by a steady increase to ~4 Å at the highest applied potential. The oxide thickness of grain 3 grows first to 2.5 Å and at a slower rate to ~3.5 Å at the highest applied potential. The results for 10 grains are shown in Fig. S7.

EC-NAPXPS

The 2D-SOR study presented above and in ref. 32 suggests an oxide/hydroxide growth at the surface of each grain, but as 2D-SOR has no chemical sensitivity, direct evidence is lacking. For this, we turned to spatially resolved EC-NAPXPS. Au

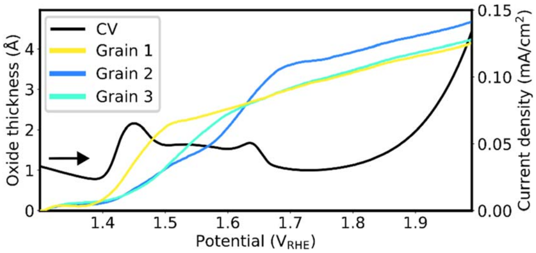

Fig. 6 Oxide thicknesses derived from the change in reflectance. Only the forward scan of the CV is shown, and the black arrow indicates scan direction.

4f core level XPS spectra for grains 1–3 measured at different potentials, and their deconvolution, are presented in Fig. 7. At open circuit potential (OCP) conditions (0.91 V_{RHE}), the bulk Au doublet components of Au $4f_{7/2}$ and Au $4f_{5/2}$ are observed at ∼84.0 eV and ∼87.6 eV, respectively. At the highest applied potential of 1.7 V_{RHE}, new components shifted by about +1.5 eV relative to the bulk peaks are observed. We assign these peaks to the existence of a Au oxide or hydroxide species.[46,47] In addition, new components shifted by −0.7 eV are assigned to Au atoms at the interface underneath the oxide/hydroxide, as observed in gas-phase studies of the oxidation of metals.[48–54] Surprisingly, this interface component appears for grains 2 and 3 at 1.4 V_{RHE}, though no oxide/hydroxide is present. We speculate that at 1.4 V_{RHE}, an ultrathin oxide/hydroxide is formed, but is unstable[46,55,56] due to a combination of beam damage and residual gas reduction while being brought out of the electrolyte. The resulting surface is therefore rough since diffusion of the remaining Au from the oxide/hydroxide is limited at room temperature, leading to under-coordinated surface atoms that exhibit a lower binding energy than that of the bulk Au.[48,56,57] Other explanations could be possible, but will not be discussed further in the present contribution.

Focusing on the development of the oxide/hydroxide components at +1.5 eV relative to the bulk, the different grains show slightly different behaviours. Grain 1 shows an oxide/hydroxide peak before grains 2 and 3, at 1.4 V_{RHE}. At 1.5 V_{RHE}, grains 2 and 3 also show the oxide/hydroxide components. These oxide/hydroxide components increase in intensity with increasing polarising potentials up to 1.7 V_{RHE}, indicating the formation of a complete thin oxide/hydroxide film.

By taking the intensity ratios of the fitted components of metallic bulk Au and oxide/hydroxide, assumed as Au_2O_3, the oxide/hydroxide thicknesses can be

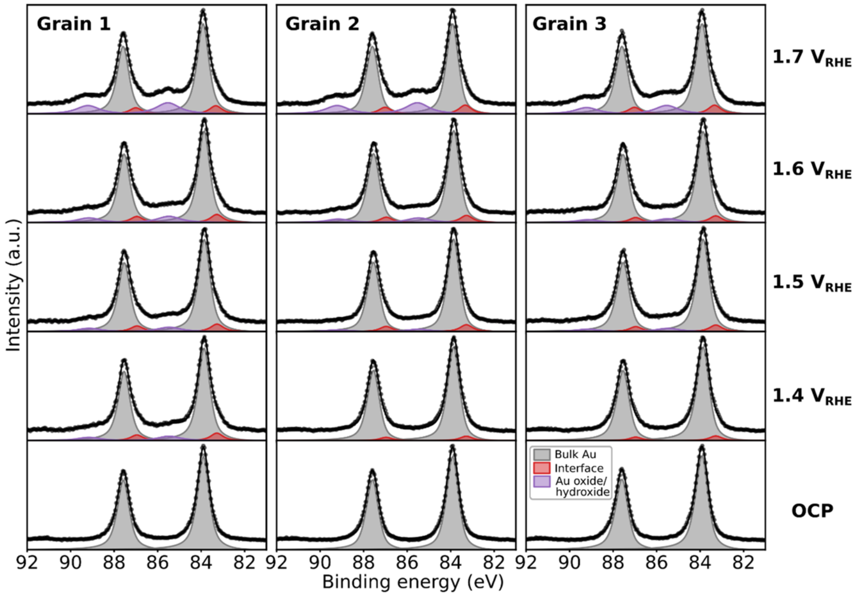

Fig. 7 Fitted XPS spectra of Au 4f core level at different EC conditions in 0.05 M H_2SO_4. The spectra are Shirley background subtracted.

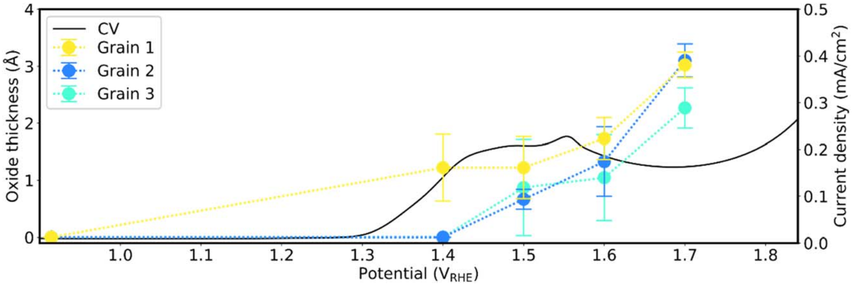

Fig. 8 Oxide thickness of Au_2O_3 (dotted lines and solid dots with error bars), derived from the intensity ratio between the Au oxide/hydroxide and bulk Au peaks from the fitted XPS spectra as a function of potential together with the forward direction of the CV (black line). The potential range of the CV was 0.25–1.85 V_{RHE} at 50 mV s^{-1}.

estimated as shown in Fig. 8. Details of the calculation, and thicknesses using $HAuO_2$, are described in SI Section 7. A CV measurement taken prior to applying the various polarisation potentials is overlaid to indicate the broad Au oxidation peak. Although grain 1 is initially oxidised at 1.4 V_{RHE} with an oxide/hydroxide film of ~1.2 Å, there is no increase in the thickness until beyond the broad Au-oxidation peak at 1.6 V_{RHE} to ~1.7 Å. Grain 3 exhibits a similar behaviour as grain 1, with a thickness of ~0.9 Å at 1.5 V_{RHE}, and ~1.0 Å at 1.6 V_{RHE}. In contrast, the oxide/hydroxide thickness of grain 2 increases in a linear fashion, from ~0.7 Å at 1.5 V_{RHE} to ~1.3 Å at 1.6 V_{RHE}. The values reported here indicate that less than a single layer of oxide/hydroxide (~2 Å) is formed on the various grains across the oxidation peaks. At the highest applied potential of 1.7 V_{RHE}, the oxide/hydroxide thicknesses of the three grains are estimated to be ~3.0 Å, ~3.1 Å, and ~2.3 Å, respectively. Between 1.6 and 1.8 V_{RHE}, the CV shows no significant change in anodic current, suggesting no new surface reactions are taking place. The increase in anodic current past 1.8 V_{RHE} marks the onset of OER, but no measurements were recorded at higher polarisation potentials.

TSXRD

Prior to the SXRD measurements, the surface was mapped with TGIXRD with the result shown in Fig. 9a, in relatively good agreement with the map from EBSD in Fig. 4a. This diffraction map provided coordinates for the COM positions of the grains, enabling fast measurements. Furthermore, it was used in the selection of the CTRs studied for each grain as further discussed in SI Section 1. Since the expected oxide/hydroxide is amorphous[44] and will not be visible with diffraction, the focus here will be the changes in the Au surface structure, observed by following the changes in a selected CTR for each grain. The selected CTRs are shown as magnified detector images in Fig. 9b (see Fig. S3 for full images). For the intensities reported in Fig. 9, the selected CTRs were measured individually during separate CVs to maximise the time resolution. The intensity far from the corresponding Bragg spot was used as a region of interest as defined in Fig. 9 and a background area of the same size was subtracted to compensate for any fluctuations in general intensity.

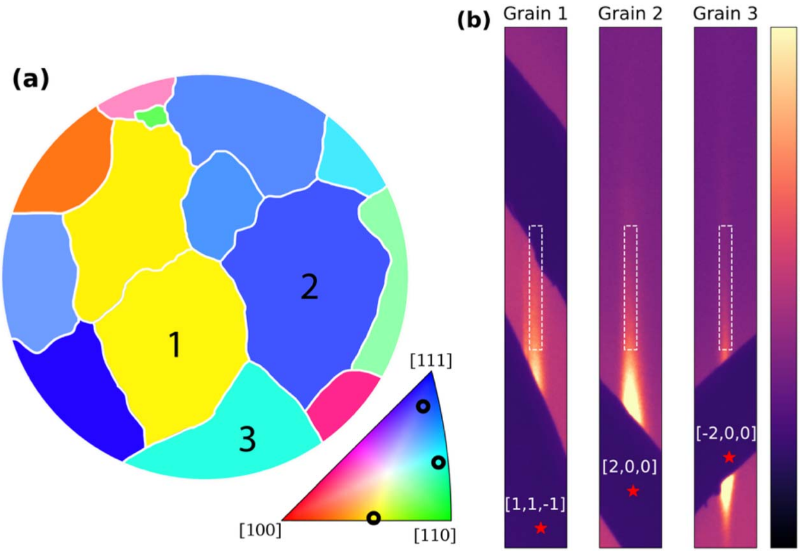

Fig. 9 (a) The grain map from TGIXRD with the grains of interest marked. (b) A magnified section of the detector image as the maximum intensity registered for each pixel during the 4° rotation for each grain (full image in Fig. S3). The COM position of the corresponding Bragg reflection (red) is hidden by the Pb mask and labelled in bulk coordinates. The white box marks the region of interest defining the CTR intensity in Fig. 10. The region of interest begins 1 $Å^{-1}$ (grain 1), 2 $Å^{-1}$ (grain 2), and 0.3 $Å^{-1}$ (grain 3) from the corresponding Bragg reflection.

In Fig. 10a, the normalised intensity variation of the CTRs over time together with the CV is shown. Before the oxidation peak, the three grains show different smaller changes. Grain 1 has a slowly decreasing intensity, grain 2 has an increasing intensity and the intensity of grain 3 remains constant. A similar but opposite behaviour for the corresponding intensities is observed after the reduction peak. The initial increase in intensity for grain 2 could be the lifting of a reconstruction,[44] with a corresponding formation after the reduction, but with the lack of visible SLRs, this cannot be confirmed.

As the potential is increased to that of the oxidation peak (1.3–1.4 V_{RHE}), a reduction in the intensities for all grains is observed. A small shift between the drop in intensity is observed, in which grain 1 has the earliest onset followed by grains 2 and 3. This variation in oxidation onset is also seen in the potential steps measured with scanning SXRD (Fig. S4). Increasing the potential further, grain 2 has a second oxidation step. This is all in agreement with the observations in the 2D-SOR.

Just after the onset of oxidation in Fig. 10a, there is an initial minimum in CTR intensity for grains 1 and 3, followed by a slight intensity increase. Later, at potentials just prior to the reduction peak, the intensity decreases sharply for grains 1 and 2, and slightly for grain 3 before the sharp increase at the reduction. For oxidation to occur, movement of Au atoms relative to the equilibrium position is required. What we observe clearly is that there are CTR intensity minima at both the oxidation onset and oxidation reduction which could indicate that there

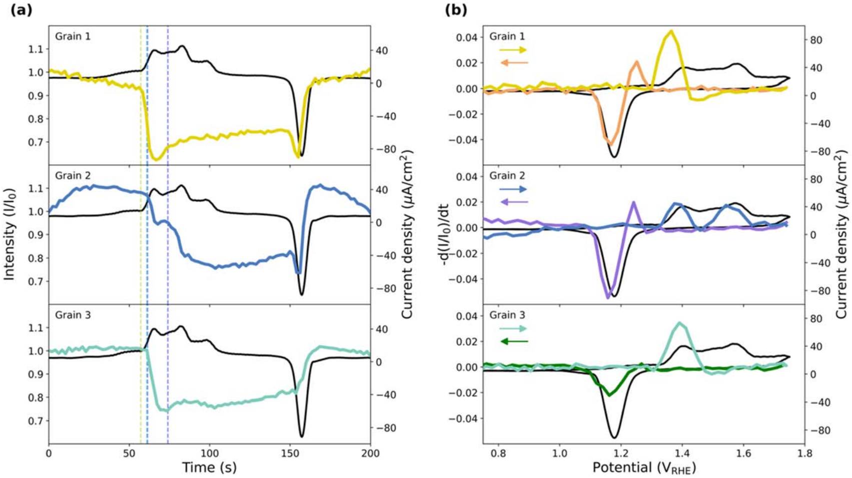

Fig. 10 (a) The intensity variation in the region of interest defined in Fig. 9a (coloured) as a function of time together with the CV (black). The intensity is normalised with the CTR intensity at $t = 0$ s. The dashed lines indicate the last timestamp before the sharp intensity drop. (b) The negative time derivative of the normalized CTR intensity as a function of potential together with the CV. The colours of the intensity during the forward and backward sweep have been separated as indicated by the arrows. The potential range of the CV was 0.2–1.75 V_{RHE} at 10 mV s^{-1} and performed in 0.05 M H_2SO_4.

is a maximum in disorder as the oxide/hydroxide is initially formed and when it is reduced.

To further facilitate the comparison of the CTR behaviour with the CV and the 2D-SOR behaviour, the negative time derivative of the normalised intensity is plotted against the CV potential in Fig. 10b, where the shift in onset potential is further shown. Here, the decrease in the intensity, observed close to the reduction peak in grains 1 and 2 in Fig. 10a, appears as a sharp peak just before the reduction peak in the return scan.

Discussion

In this contribution we have used a polycrystalline Au sample with grains large enough for us to study the electro-oxidation and reduction of the different grains in the same EC environment. To do this, we have used 2D-SOR, EC-NAPXPS and TSXRD, combined with EC techniques. We have shown that the CV from the polycrystalline Au surface exhibits a broad oxidation peak, and that the peak shape can be qualitatively reproduced by the combination of derivatives of the surface signals from 2D-SOR applied to individual grains. We have also shown using EC-NAPXPS that the changes in the 2D-SOR and TSXRD signal are due to the oxidation of the electrode into a Au oxide/hydroxide, and that the different grains oxidise at different potentials. The change in the 2D-SOR reflectance signal is therefore due to changes in the refractive indices from the Au to the oxide/hydroxide thin film, while the change of the TSXRD signal is due to the roughening of the surface caused by the electro-oxidation.

The TSXRD results confirm what has previously been seen for similar SXRD measurements of single crystals, that the CTRs decrease in intensity as the oxide forms at the surface.[44] No SLR of the oxide/hydroxide is detected, since the EC formed oxide/hydroxide is amorphous due to limited diffusion at room temperature and thus not visible with diffraction. Furthermore, no initial surface reconstructions are observed, despite the CTR behaviour indicating that this can be the case for grain 2. This absence does not necessarily imply that such reconstructions are absent, but rather that their signal may be too weak to detect. Furthermore, it is possible that the surface preparation did not remove all roughening of the surface. That the initial CTR intensity is recovered fully after CV can indicate that the surface prior to the sweep was already rough, since there can be significant roughening after the reduction after just one cycle.[14] In addition, in the TSXRD, there is a surprising decrease in the intensity (seen as an increase in the derivative) just after oxidation and before the reduction of the oxide/hydroxide, which is not observed in the CV, EC-NAPXPS or 2D-SOR data. We speculate that this is a disorder at the interface observable in the TSXRD but not in the 2D-SOR caused by the restructuring of the Au atoms and the dissolution increase that has been observed for a Au(111) surface.[10]

The results from the 2D-SOR and TSXRD show similar behaviour, where grain 1 show the earliest onset of oxidation, closely followed by grains 2 and 3. This is also observed and confirmed in the EC-NAPXPS measurements. Furthermore, a two-step oxidation is shown for grain 2 with both 2D-SOR and TSXRD. As further discussed in SI Section 8, there are some variations in the setups and EC procedure of the different methods, hindering complete comparability of the CVs. However, the changes in the 2D-SOR and TSXRD signal relative to their respective CV features show that there is a slightly earlier onset for the TSXRD as compared to the 2D-SOR at oxidising potentials. This could be understood by the TSXRD detecting a roughening of the surface before any oxide/hydroxide with a reasonable refractive index can form. The short X-ray wavelength is able to detect atomic scale roughening events, while the much longer red-light LED wavelength used for the 2D-SOR is unable to do this. Despite these differences, we observe for all grains that after an initial fast oxidation event, the oxidation rate slows down considerably. This is a classic behaviour for the formation of a self-limited, passive oxide film.[50,58–62]

The 2D-SOR and the EC-NAPXPS provides data which can be translated into oxide/hydroxide thicknesses and is summarised in Table 1, and Fig. 6 and 8 are

Table 1 Summary of oxide thicknesses (Å) estimated from 2D-SOR and EC-NAPXPS, assuming the Au oxide/hydroxide is Au_2O_3

Oxide thickness (Å)								
Potential (V_{RHE})	1.4		1.5		1.6		1.7	
Method	XPS	SOR	XPS	SOR	XPS	SOR	XPS	SOR
Grain 1	1.2	0.3	1.2	2.1	1.7	2.5	3.0	3.0
Grain 2	0	0.2	0.7	1.0	1.3	2.1	3.1	3.6
Grain 3	0	0.2	0.9	1.1	1.1	2.4	2.3	3.0

presented side-by-side for comparison in Fig. S11. Excluding the 1.4 V_{RHE}, our measurements agree qualitatively, though we note an underestimation of the XPS thickness, which could be due to a slow reduction of the oxide in the *ex situ* gas-phase H_2O environment during the EC-NAPXPS measurements. The estimated thickness values are very sensitive to the exact measurement procedure. For instance, the rapid oxidation of grain 1 between 1.4 V_{RHE} and 1.5 V_{RHE} is observed with 2D-SOR, but not EC-NAPXPS. Here, it can be noted that also the EC-NAPXPS shows a step with accelerated oxide/hydroxide growth for grain 2 at higher potentials. Between 1.4 V_{RHE} and 1.6 V_{RHE}, the estimated oxide/hydroxide thicknesses correspond to less than a single layer of oxide/hydroxide ($\sim$2 Å), suggesting that the oxide/hydroxide does not fully cover the surface of the grains. Only well above the oxidation peaks, a complete 2.3–3.1 Å oxide/hydroxide film is found for all grains, differing with previous X-ray reflectivity work measuring oxide thicknesses of Au(111) and Au(100) above the respective oxidation peaks, which is modelled with two oxide/hydroxide layers and a thickness of around 5.5 Å.[63]

From the measurements, it is clear that the surface orientation affects the surface oxidation. This is further shown in SI Section 4, where the 2D-SOR evaluation from 10 grains displays clear similarities in oxidation behaviour for grains of similar surface orientation. Grain 1 is a (210) surface, giving rise to a large number of small steps and a more “open” surface, which could explain the earlier onset of the oxidation compared to grains 2 and 3, which as (554) and (552) surfaces are more “closed” with larger terraces. This can be compared to the relatively later onset of oxidation at a (111) single crystal compared to the more “open” (100) and (110) surfaces. (111) surfaces have previously been shown to require higher overpotential for the oxidation reaction compared to the other low-index planes.[5,45,64,65] Grain 2 shows a two-step oxidation behaviour both in 2D-SOR and TSXRD. This grain has a (554) orientation which is quite close to a (111) surface with relatively large terraces separated by steps. One possible reason for the two-step oxidation is the formation of a first thin self-limited oxide/hydroxide that hinders the subsequent oxidation until the system passes a threshold at which further oxidation is enabled. This behaviour has been observed previously for gas-phase oxidation[63,65] as well as for Au(111) in electrochemistry.[10] Alternatively, it could be a 1D oxide/hydroxide forming at the steps, limiting the formation of the 2D oxide/hydroxide at the (111) terraces as previously observed in gas-phase oxidation.[66] Terrace size dependent oxidation behaviour has previously been studied where the secondary oxidation peak is more prominent for the surface orientations closer to (111) such as the (554) orientation.[67] This behaviour of the relative intensity of the first and secondary oxidation peak can also be noted in the 2D-SOR measurements for all grains where the secondary peak is dependent on the (111) terrace size for each grain (Fig. S6). Since grain 3 has much smaller (111) terraces compared to grain 2, making the less coordinated atoms at the steps the most prominent feature. Thus, a separation of terrace and step oxidation is not expected.

Understanding of the system is strengthened by the combination of different techniques, the simplest of which is 2D-SOR, which provides high temporal and spatial resolution for *operando* measurements but requires other techniques to determine the cause of the changes in reflectance. EC-NAPXPS has excellent chemical and surface sensitivity, and allows for quantitative analysis, but can in the present case not provide time-resolved or fully *operando* measurements.

Finally, TSXRD can provide very surface sensitive structural information at the atomic scale from *operando* measurements, but since diffraction is only sensitive to periodic structures, it cannot directly detect amorphous oxides/hydroxides, and quantitative analysis is not trivial.

Conclusions

We have used three different surface sensitive techniques, 2D-SOR, EC-NAPXPS and TSXRD, to study the behaviour of grains with different surface orientations of a polycrystalline Au sample during electro-oxidation/reduction experiments. The results can be used to explain the broad oxidation peak observed in the CV, consisting of contributions from several grains. We have shown qualitative agreement between the different techniques in terms of relative oxidation onsets and oxide/hydroxide thicknesses at the different grains. The study demonstrates that it is possible to follow dynamic changes of electrode surfaces during CV in harsh environments. Furthermore, the combination of techniques provides complementary information of the system since they probe different surface properties. Here we demonstrate the complexity of the polycrystalline electrode, and how the different contributions can be disentangled. Our approach offers insight into the dynamic behaviour of a more realistic electrode, enabling grain-resolved understanding of the electro-oxidation process.

Author contributions

AT and HS contributed equally to this work. Conceptualisation: HS, AL, JG, EdL; data curation: AT, HS, AL; investigation: AT, HS, AG, EsL, AL, CB, LRM, UK, JK, EdL; methodology: AT, HS, AL, JG, JK, EdL; visualisation: AT, HS, AL, UK; writing – original draft: AT, HS, EdL; writing – review & editing: all authors; funding acquisition: EdL, JG, JK; supervision: JG, EdL.

Conflicts of interest

There are no conflicts to declare.

Data availability

The data that support the findings of this study are openly available by contacting the corresponding authors. The authors confirm that the data supporting the findings of this study are available within the article and the supplementary information (SI). Supplementary information: explanation of the CTR selection for the SXRD measurements, sequential SXRD measurements of all three grains during potential steps, explanation of the 2D-SOR oxide thickness calculation, 2D-SOR of all grains of the polycrystalline Au, details of the EC measurement procedure for the EC-NAPXPS experiment, EC-NAPXPS fitting parameters, explanation of the EC-NAPXPS oxide thickness calculation, differences in EC between the experiments, full CV showing the feature related to H_2O_2 oxidation, comparison of oxide thickness obtained from EC-NAPXPS and 2D-SOR. See DOI: https://doi.org/10.1039/d5fd00129c.

Acknowledgements

Financial support is acknowledged from the Swedish Research Council (2020-06154 E. L., 2022-03041 E. L., 2022-04363 J. K., 2017-04840 J. K, 2021-05846 J. G., 2024-00351 A. L.). This work was partially supported by the Wallenberg Initiative Materials Science for Sustainability (WISE) funded by the Knut and Alice Wallenberg Foundation and the Crafoord Foundation. We acknowledge MAX IV Laboratory for time on Beamline HIPPIE under Proposal 20231082. Research conducted at MAX IV, a Swedish national user facility, is supported by the Swedish Research Council under Contract 2018-07152, the Swedish Governmental Agency for Innovation Systems under Contract 2018-04969, and Formas under Contract 2019-02496. We acknowledge DESY (Hamburg, Germany), a member of the Helmholtz Association HGF, for the provision of experimental facilities. Parts of this research were carried out at PETRA III, and we would like to thank Zoltán Hegedüs, Malte Blankenburg, and Sven Gutschmidt for assistance in using the Swedish High-Energy X-ray Materials Science Beamline (P21.2). Beamtime was allocated under proposal I-20240196 EC.

Notes and references

1 H. Wang, Z. Yan, F. Cheng and J. Chen, *Adv. Sci.*, 2024, **11**, 2401652.

2 Z. W. Seh, J. Kibsgaard, C. F. Dickens, I. Chorkendorff, J. K. Nørskov and T. F. Jaramillo, *Science*, 2017, **355**, eaad4998.

3 F. Hess and H. Over, *ACS Catal.*, 2023, **13**, 3433–3443.

4 R. Kötz, S. Stucki, D. Scherson and D. M. Kolb, *J. Electroanal. Chem. Interfacial Electrochem.*, 1984, **172**, 211–219.

5 X. Xu, M. Kang, S. Yan, E. Daviddi, G. West, D. Valavanis, O. J. Wahab and P. R. Unwin, *ACS Electrochem.*, 2025, **1**, 1852–1862.

6 J. H. K. Pfisterer, M. Baghernejad, G. Giuzio and K. F. Domke, *Nat. Commun.*, 2019, **10**, 5702.

7 B. Steinhauser, C. Vidal, R. A. Barb, J. Heitz, A. I. Mardare, A. W. Hassel, C. Hrelescu and T. A. Klar, *J. Phys. Chem. C*, 2018, **122**, 4565–4571.

8 T. Binninger, R. Mohamed, K. Waltar, E. Fabbri, P. Levecque, R. Kötz and T. J. Schmidt, *Sci. Rep.*, 2015, **5**, 12167.

9 A. Larsson, A. Grespi, G. Abbondanza, J. Eidhagen, D. Gajdek, K. Simonov, X. Yue, U. Lienert, Z. Hegedüs, A. Jeromin, T. F. Keller, M. Scardamaglia, A. Shavorskiy, L. R. Merte, J. Pan and E. Lundgren, *Adv. Mater.*, 2023, **35**, 2304621.

10 A. Grespi, A. Larsson, A. Ti, V. Briega-Martos, E. Lira, U. Küst, G. Abbondanza, J. Manidi, S. Cherevko, A. Shavorskiy, M. Scardamaglia, M. Ramakrishnan, J. Just, L. R. Merte and E. Lundgren, *ChemRxiv*, 2025, preprint, DOI: 10.26434/CHEMRXIV-2025-149TJ.

11 T. Fuchs, J. Drnec, F. Calle-Vallejo, N. Stubb, D. J. S. Sandbeck, M. Ruge, S. Cherevko, D. A. Harrington and O. M. Magnussen, *Nat. Catal.*, 2020, **3**, 754–761.

12 O. M. Magnussen, J. Drnec, C. Qiu, I. Martens, J. J. Huang, R. Chattot and A. Singer, *Chem. Rev.*, 2024, **124**, 629–721.

13 M. Ruge, J. Drnec, B. Rahn, F. Reikowski, D. A. Harrington, F. Carlà, R. Felici, J. Stettner and O. M. Magnussen, *J. Electrochem. Soc.*, 2017, **164**, H608–H614.

14 C. Stumm, S. Grau, F. D. Speck, F. Hilpert, V. Briega-Martos, K. Mayrhofer, S. Cherevko, O. Brummel and J. Libuda, *J. Phys. Chem. C*, 2021, **125**, 22698–22704.

15 S. Behjati and M. T. M. Koper, *J. Phys. Chem. C*, 2024, **128**, 19024–19034.

16 T. Moser, F. Valls Mascaró and J. Kunze-Liebhäuser, *J. Phys. Chem. C*, 2025, **129**, 14411–14417.

17 A. Björling, E. Herrero and J. M. Feliu, *J. Phys. Chem. C*, 2011, **115**, 15509–15515.

18 J. G. Wang, W. X. Li, M. Borg, J. Gustafson, A. Mikkelsen, T. M. Pedersen, E. Lundgren, J. Weissenrieder, J. Klikovits, M. Schmid, B. Hammer and J. N. Andersen, *Phys. Rev. Lett.*, 2005, **95**, 256102.

19 F. V. Mascaró, M. T. M. Koper and M. J. Rost, *Electrochim. Acta*, 2024, **506**, 145014.

20 Y. Wang, S. A. Skaanvik, X. Xiong, S. Wang and M. Dong, *Matter*, 2021, **4**, 3483–3514.

21 P. Winkler, J. Zeininger, Y. Suchorski, M. Stöger-Pollach, P. Zeller, M. Amati, L. Gregoratti and G. Rupprechter, *Nat. Commun.*, 2021, **12**, 69.

22 Y. Ning, Q. Fu, Y. Li, S. Zhao, C. Wang, M. Breitschaft, S. Hagen, O. Schaff and X. Bao, *Ultramicroscopy*, 2019, **200**, 105–110.

23 A. Larsson, K. Simonov, J. Eidhagen, A. Grespi, X. Yue, H. Tang, A. Delblanc, M. Scardamaglia, A. Shavorskiy, J. Pan and E. Lundgren, *Appl. Surf. Sci.*, 2023, **611**, 155714.

24 J. Clavilier, R. Faure, G. Guinet and R. Durand, *J. Electroanal. Chem. Interfacial Electrochem.*, 1980, **107**, 205–209.

25 A. J. Schwartz, M. Kumar, B. L. Adams and D. P. Field, *Electron Backscatter Diffraction in Materials Science*, Springer US, 2009.

26 W. G. Onderwaater, A. Taranovskyy, G. M. Bremmer, G. C. Van Baarle, J. W. M. Frenken and I. M. N. Groot, *Rev. Sci. Instrum.*, 2017, **88**, 023704.

27 J. Zhou, S. Blomberg, J. Gustafson, E. Lundgren and J. Zetterberg, *J. Phys. Chem. C*, 2017, **121**, 23511–23519.

28 J. Zetterberg, A. Larsson, A. Grespi, S. Pfaff, L. Rämisch, L. R. Merte and E. Lundgren, *J. Phys.: Condens. Matter*, 2025, **37**, 133003.

29 L. Rämisch, S. M. Gericke, S. Pfaff, E. Lundgren and J. Zetterberg, *Appl. Surf. Sci.*, 2022, **578**, 152048.

30 A. Larsson, M. Vorobyova, S. Pfaff, G. Abbondanza, J. Pan, J. Zetterberg and E. Lundgren, *J. Phys. Chem. C*, 2023, **127**, 21871–21877.

31 S. Pfaff, A. Larsson, D. Orlov, L. Rämisch, S. M. Gericke, E. Lundgren and J. Zetterberg, *ACS Appl. Mater. Interfaces*, 2024, **16**, 444–453.

32 S. Pfaff, A. Larsson, D. Orlov, G. S. Harlow, G. Abbondanza, W. Linpé, L. Rämisch, S. M. Gericke, J. Zetterberg and E. Lundgren, *ACS Appl. Mater. Interfaces*, 2021, **13**, 19530–19540.

33 S. Zhu, M. Scardamaglia, J. Kundsen, R. Sankari, H. Tarawneh, R. Temperton, L. Pickworth, F. Cavalca, C. Wang, H. Tissot, J. Weissenrieder, B. Hagman, J. Gustafson, S. Kaya, F. Lindgren, I. Kallquist, J. Maibach, M. Hahlin, V. Boix, T. Gallo, F. Rehman, G. D'Acunto, J. Schnadta and A. Shavorskiy, *J. Synchrotron Radiat.*, 2021, **28**, 624–636.

34 X. Yue, A. Larsson, H. Tang, A. Grespi, M. Scardamaglia, A. Shavorskiy, A. Krishnan, E. Lundgren and J. Pan, *Corros. Sci.*, 2023, **214**, 111018.

35 M. Newville, R. Otten, A. Nelson, T. Stensitzki, A. Ingargiola, D. Allan, A. Fox, F. Carter, Michał, R. Osborn, D. Pustakhod, Ineuhaus, S. Weigand, A. Aristov, Glenn, C. Deil, Mgunyho, Mark, A. L. R. Hansen, G. Pasquevich, L. Foks, N. Zobrist, O. Frost, Stuermer, Azelcer, A. Polloreno, A. Persaud, J. H. Nielsen, M. Pompili and P. Eendebak, lmfit/lmfit-py (1.2.2), *Zenodo*, 2023, DOI: 10.5281/zenodo.8145703.

36 I. K. Robinson, *Phys. Rev. B: Condens. Matter Mater. Phys.*, 1986, **33**, 3830.

37 R. Felici, *Characterization of Materials*, 2012, pp. 1424–1442.

38 Z. Hegedüs, T. Müller, J. Hektor, E. Larsson, T. Bäcker, S. Haas, A. L. C. Conceiçao, S. Gutschmidt and U. Lienert, *IOP Conf. Ser.: Mater. Sci. Eng.*, 2019, **580**, 012032.

39 W. Linpé, G. S. Harlow, A. Larsson, G. Abbondanza, L. Rämisch, S. Pfaff, J. Zetterberg, J. Evertsson and E. Lundgren, *Rev. Sci. Instrum.*, 2020, **91**, 044101.

40 M. L. Foresti, A. Pozzi, M. Innocenti, G. Pezzatini, F. Loglio, E. Salvietti, A. Giusti, F. D'Anca, R. Felici and F. Borgatti, *Electrochim. Acta*, 2006, **51**, 5532–5539.

41 H. Sjö, A. Shabalin, U. Lienert, J. Hektor, A. Schaefer, P. A. Carlsson, C. Alwmark and J. Gustafson, *Surf. Sci.*, 2025, **754**, 122693.

42 D. N. Johnstone, B. H. Martineau, P. Crout, P. A. Midgley and A. S. Eggeman, *J. Appl. Crystallogr.*, 2020, **53**, 1293–1298.

43 A. M. Gómez-Marín, A. Boronat and J. M. Feliu, *Russ. J. Electrochem.*, 2017, **53**, 1153–1168.

44 W. Linpé, L. Rämisch, G. Abbondanza, A. Larsson, S. Pfaff, L. Jacobse, J. Zetterberg, L. Merte, A. Stierle, Z. Hegedues, U. Lienert, E. Lundgren and G. S. Harlow, *J. Electrochem. Soc.*, 2021, **168**, 096511.

45 L. A. Kibler, *Preparation and Characterization of Noble Metal Single Crystal Electrode Surfaces*, International Society of Electrochemistry, Ulm, 2003.

46 B. Koslowski, H. G. Boyen, C. Wilderotter, G. Kästle, P. Ziemann, R. Wahrenberg and P. Oelhafen, *Surf. Sci.*, 2001, **475**, 1–10.

47 K. Juodkazis, J. Juodkazyte, V. Jasulaitiene, A. Lukinskas and B. Šebeka, *Electrochem. Commun.*, 2000, **2**, 503–507.

48 C. Berg, S. Raaen, A. Borg, J. N. Andersen, E. Lundgren and R. Nyholm, *Phys. Rev. B: Condens. Matter Mater. Phys.*, 1993, **47**, 13063.

49 M. Todorova, E. Lundgren, V. Blum, A. Mikkelsen, S. Gray, J. Gustafson, M. Borg, J. Rogal, K. Reuter, J. N. Andersen and M. Scheffler, *Surf. Sci.*, 2003, **541**, 101–112.

50 J. Gustafson, A. Mikkelsen, M. Borg, E. Lundgren, L. Köhler, G. Kresse, M. Schmid, P. Varga, J. Yuhara, X. Torrelles, C. Quirós and J. N. Andersen, *Phys. Rev. Lett.*, 2004, **92**, 126102.

51 J. Gustafson, A. Mikkelsen, M. Borg, J. N. Andersen, E. Lundgren, C. Klein, W. Hofer, M. Schmid, P. Varga, L. Köhler, G. Kresse, N. Kasper, A. Stierle and H. Dosch, *Phys. Rev. B: Condens. Matter Mater. Phys.*, 2005, **71**, 115442.

52 E. Lundgren, A. Mikkelsen, J. N. Andersen, G. Kresse, M. Schmid and P. Varga, *J. Phys.: Condens. Matter*, 2006, **18**, R481.

53 N. M. Martin, J. Knudsen, S. Blomberg, J. Gustafson, J. N. Andersen, E. Lundgren, H. H. Ingelsten, P. A. Carlsson, M. Skoglundh, A. Stierle and G. Kresse, *Phys. Rev. B: Condens. Matter Mater. Phys.*, 2011, **83**, 125417.

54 S. Blomberg, U. Hejral, M. Shipilin, S. Albertin, H. Karlsson, C. Hulteberg, P. Lömker, C. Goodwin, D. Degerman, J. Gustafson, C. Schlueter, A. Nilsson, E. Lundgren and P. Amann, *ACS Catal.*, 2021, **11**, 9128–9135.

55 A. Y. Klyushin, T. C. R. Rocha, M. Hävecker, A. Knop-Gericke and R. Schlögl, *Phys. Chem. Chem. Phys.*, 2014, **16**, 7881–7886.

56 E. Lira, A. Grespi, N. Paoletti, A. Ti, A. M. Rodriguez, A. Larsson, L. R. Merte and E. Lundgren, *Rev. Sci. Instrum.*, 2026, **97**, 033903.

57 J. Gustafson, M. Borg, A. Mikkelsen, S. Gorovikov, E. Lundgren and J. N. Andersen, *Phys. Rev. Lett.*, 2003, **91**, 056102.

58 N. Cabrera and N. F. Mott, *Rep. Prog. Phys.*, 1949, **12**, 163.

59 F. P. Fehlner and N. F. Mott, *Oxid. Met.*, 1970, **2**, 59–99.

60 J. W. Schultze and M. M. Lohrengel, *Electrochim. Acta*, 2000, **45**, 2499–2513.

61 J. Evertsson, F. Bertram, F. Zhang, L. Rullik, L. R. Merte, M. Shipilin, M. Soldemo, S. Ahmadi, N. Vinogradov, F. Carlà, J. Weissenrieder, M. Göthelid, J. Pan, A. Mikkelsen, J. O. Nilsson and E. Lundgren, *Appl. Surf. Sci.*, 2015, **349**, 826–832.

62 A. Larsson, G. D'Acunto, M. Vorobyova, G. Abbondanza, U. Lienert, Z. Hegedüs, A. Preobrajenski, L. R. Merte, J. Eidhagen, A. Delblanc, J. Pan and E. Lundgren, *J. Alloys Compd.*, 2022, **895**, 162657.

63 T. Kondo, J. Morita, K. Hanaoka, S. Takakusagi, K. Tamura, M. Takahasi, J. N. I. Mizuki and K. Uosaki, *J. Phys. Chem. C*, 2007, **111**, 13197–13204.

64 A. Hamelin, *J. Electroanal. Chem.*, 1996, **407**, 1–11.

65 M. Shipilin, J. Gustafson, C. Zhang, L. R. Merte, A. Stierle, U. Hejral, U. Ruett, O. Gutowski, M. Skoglundh, P. A. Carlsson and E. Lundgren, *J. Phys. Chem. C*, 2015, **119**, 15469–15476.

66 J. Klikovits, M. Schmid, L. R. Merte, P. Varga, R. Westerström, A. Resta, J. N. Andersen, J. Gustafson, A. Mikkelsen, E. Lundgren, F. Mittendorfer and G. Kresse, *Phys. Rev. Lett.*, 2008, **101**, 266104.

67 A. Hamelin and A. M. Martins, *J. Electroanal. Chem.*, 1996, **407**, 13–21.